Materials Science & Engineering A 788 (2020) 139535

Contents lists available at ScienceDirect

Materials Science & Engineering A

journal homepage: http://www.elsevier.com/locate/msea

Mechanisms of Ti and B on improving weld metal toughness of a Nb-alloyed steel

Xun Liu [a,*], Qianying Shi [b], Mingjie Xu [c], Jiarui Kang [a], Sydnee Webb [d]

[a] Welding Engineering, Department of Material Science and Engineering, The Ohio State University, Columbus, OH, 43221, USA
[b] Department of Material Science and Engineering, University of Michigan, Ann Arbor, MI, 48109, USA
[c] Irvine Materials Research Institute, University of California Irvine, Irvine, CA, 92697, USA
[d] Lincoln Electric, Euclid, OH, 44117, USA

ARTICLE INFO

Keywords:
Submerged arc welding
Nb-alloyed steel
Weld metal toughness
TEM
Atom probe tomography

ABSTRACT

It is known that titanium (Ti) and boron (B) elements in the filler metal can effectively improve the toughness of high heat input welds of Nb-alloyed steels. This generally has been attributed to refinement of weld microstructure and modifications of different iron constituents in the optical microscopic length scale. To improve understanding of fundamental mechanisms and directly reveal the distribution and interactions of Ti, B, Nb and other alloying elements, in this study, atomic scale characterizations and microchemistry analysis are performed with atom probe tomography (APT) and transmission electron microscopy (TEM). Three types of welding consumables are evaluated on submerged arc welds of X70 steel, among which the Ti-B-Mo rich electrode produces the best toughness properties. In the weld from Ti-B-Mo rich electrode, significant amount of C, B and Ti is segregated along the prior austenite grain boundary (PAGB) while B is depleted adjacent to PAGB. Nb also decorates the PAGB but with a lower segregation level. This is potentially due to the lower affinity of Nb to C and B compared with Ti. In the vicinity of PAGB, Nb exists in the form of solid solution in the ferrite matrix. TEM analysis similarly shows that overall Nb is uniformly distributed throughout the weld without large scale segregation.

1. Introduction

Benefits of titanium (Ti) and boron (B) elements in the filler metal have been well recognized in effectively improving the toughness for high heat input welds of steels containing more than 0.15 wt% niobium (Nb) [1,2]. One typical application is on submerged arc welding (SAW) of Nb-alloyed pipeline steels. Ti itself has a high affiliation with O, C and N and form compounds. Dispersions of TiN precipitates retard austenite grain coarsening [3,4]. Titanium oxides serve as heterogeneous nucleation sites for acicular ferrite, which accordingly refines the final weld metal microstructure and improves toughness. In addition, Ti can react with other elements, such as Mn and Zr, to form oxide particles. These non-metallic inclusions (200-400 nm) are potent for intragranular nucleation of acicular ferrite and increase its amount [5,6]. Several studies have been performed to understand the chemistry, density and size distribution of these Ti-containing inclusions [7,8], and the potency to nucleate acicular ferrite [9].

B is known to segregate along prior austenite grain boundaries (PAGB), which lowers the PAGB energy, delays boundary ferrite nucleation [10] and increases the cohesive strength of the boundaries without causing embrittlement [11]. In addition, B can effectively enhance the hardenability of steel by suppressing the austenite to ferrite transformation temperature [12]. Several theories have been proposed to explain the accumulation of B atoms along the grain boundary. One is that B forms vacancy-B complex and segregates to PAGB through a non-equilibrium mechanism [13,14]. Adding Ti is effective to protect B from reacting with nitrogen and oxygen, which preserves its beneficial effects. With optimized Ti and B contents, maximum potency to nucleate intragranular ferrite and therefore high levels of acicular ferrite can be achieved in the microstructure [15].

Nb has been a well-recognized microalloying element to improve the strength and toughness for low carbon steels. During the thermo-mechanically controlled steel manufacturing process, Nb can exist in the form of solid solution or precipitates [16], which effectively delays austenite recrystallization and retards coarsening through solution drag [17,18] or grain boundary pinning effect. A fine acicular ferrite

* Corresponding author.
E-mail address: liu.7054@osu.edu (X. Liu).

https://doi.org/10.1016/j.msea.2020.139535
Received 11 February 2020; Received in revised form 21 April 2020; Accepted 4 May 2020
Available online 11 May 2020

microstructure can be achieved upon further cooling, which produces optimized mechanical properties of both strength and toughness [19]. Takayama [20] found that Nb enhanced the formation of Martensite-Austenite (MA) constituents over a wide range of cooling rates. Nb has a strong tendency to segregate to PAGB [21,22], dislocations and other crystal defects. Strain induced Nb precipitation has been well known and systematically modeled [23]. For processes that involve rapid cooling, for example, the strip-cast process, where the cooling rate can reach 40-60 °C/s through the austenite to ferrite transformation temperature region [24,25], ultra-fine Nb rich clusters containing 4-20 Nb atoms that resemble the Guinier-Preston zones in Al-Cu alloys are observed. These effectively improve both ductility and strength of steel [26].

With the co-existence of Ti and Nb, complex precipitates (Ti,Nb)(C, N) can form in steel, which is generally composed of a Ti-rich core and Nb-rich shell [27,28]. Tirumalasetty et al. [29] revealed the presence of (Nb,Ti)N with transmission electron microscopy (TEM), which followed a well-defined N-W orientation relationship with the ferrite matrix. (Nb, Ti)N was also found in martensite and bainite phases. The process of co-precipitating of NbC-rich precipitates on a core of TiN is explained as the following [30]: the titanium nitride particles are generated in the liquid or at a high temperature, which then serve as heterogeneous nucleation sites for Nb carbonitride or Ti carbide at lower temperature. Jia et al. [31] observed Nb containing Ti-rich carbides and described their formation involves nucleating of TiC followed by epitaxial precipitation of NbC on TiC surface. The (Ti,Nb)(C,N) precipitates showed a cubic morphology in the steel matrix [32]. Zhou and Priestner [27] found that by increasing either the N or Ti content, Nb-rich precipitates became Ti-rich during quenching of steel ingots. Nb-rich carbonitrides can also co-precipitate with weld inclusions by forming an out shell enclosing the nucleating particles.

Despite these benefits that Nb brings to steel and considerable amount of studies to understand the fundamental mechanisms of Nb during steel manufacturing processes, on the other hand, effects of Nb on weld metal toughness have been historically elusive and closely depend on the composition of the filler metal selected for the welding process. Historically in higher carbon steels, Nb was observed to promote formation of Widmanstatten ferrite, reduce grain boundary ferrite and refine acicular ferrite structures [33,34]. The first effect is detrimental to toughness while the latter two are beneficial. According to Dolby [33], if the original steel structure starts with acicular ferrites and certain amount of grain boundary ferrites, after weld dilution, Nb would promote Widmanstatten ferrite formation, which reduces the weld metal toughness. Farrar and Harrison [35] summarized that if the weld metal has low hardenability, Nb enhances side plate ferrite formation, whereas for weld metal with high hardenability, Nb increases the amount of acicular ferrite.

So far, the majority of the studies regarding Nb effects on weld metal microstructure and properties focused on the volume fraction and distribution of different iron phases and microconstituents in the optical microscopic length scale. Distributions and interactions of different elements in the weld metal and their relationship to the iron phases have not been fully elucidated. Nano-scale characterizations of Nb are mainly performed in the field of steel manufacturing, where the thermo-mechanical condition is highly different from that during welding. In this study, effects of electrode composition on the toughness of the submerged arc welds of X70 steel are comprehensively studied. X70 is one of the commonly used pipeline steels that can contain Nb levels up to 0.086 wt%. Multiscale characterizations of the weld microstructure are performed, and their relationships with the measured toughness properties are established. Distribution and morphology of the main elements, specifically B, Ti and Nb and their interactions are directly examined with atom probe tomography (APT) and TEM. Since B is the fifth lightest element and its concentration can be low in the weld metal, the chemical sensitivity and near atomic spatial resolution of APT makes it an advantageous approach to resolve B distribution.

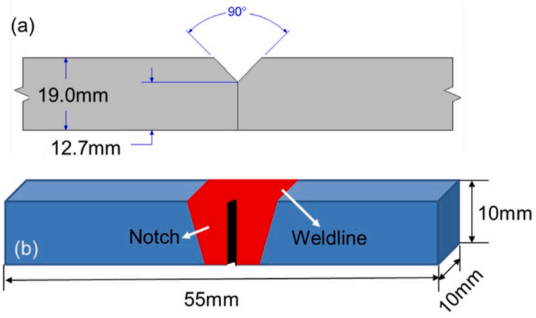

Fig. 1. (a) Schematic of the SAW weld sample preparation; (b) Dimensions and notch location of the CVN test specimen.

2. Experimental details

Two plates of X70 steel were butt configured and beveled with a V-groove geometry on top of the faying surface. Detailed dimensions are provided in Fig. 1(a). Tandem submerged arc welding with standard basic flux was performed with an average heat input rate of around 111.6kJ/in. Three types of electrodes, including regular, Mn-Si rich and Ti-B-Mo rich ones were also selected and their effects on weld metal toughness compared.

Impact toughness of the weld was evaluated with standard Charpy V-notch (CVN) impact tests. For the impact test samples, all the weld reinforcement on the top surface was machined off, and the top surface of the CVN is aligned with the top surface of the plate. The V notch is prepared via electrical discharge machining (EDM) in the center of the weld and oriented perpendicular to the weldline, as illustrated in Fig. 1 (b). Impact tests were performed at -18 °C (0 °F), -29 °C (-20 °F) and -40 °C (-40 °F) with 5 repetitions at each temperature. Hardness of the weld metal was measured with indentations of a 10 kg load and 10-s dwell time. 5 indentations are performed at random locations in the weld and the average value is reported for comparison.

Bulk chemical compositions of the weld are measured by arc spark optical emission spectroscopy (OES). Chemistry of the welds obtained from the three electrodes are provided in Table 1 in weight percent (wt %). Main alloying elements that have different compositions among the three electrodes are highlighted.

Metallurgical samples of the weld were sectioned perpendicular to the weld line, which are then ground, polished and etched with Nital solution. Overview of the weld metal microstructure was examined through optical microscope. Atom probe tomography (APT) samples were prepared with a FEI Helios Nanolab microscope with scanning electron microscopy (SEM) and focused ion beam (FIB) capabilities, which allows site-specific sample extraction at desired locations. Each individual sample was then sharpened with annular ion milling to a conical tip with an end diameter of 30-40 nm. APT data was collected on a Cameca LEAP 5000XR instrument operated in the laser-pulsing mode with a pulse energy of 50 pJ at a detection rate of 1.0%, and a specimen temperature of 50 K. Data analysis and 3D tomographic reconstruction were performed with the Cameca Integrated Visualization and Analysis Software (IVAS 3.8.2) package. In the spectrum, the possible evaporation of $^{14}N^{1+}$ signal, which overlaps with $^{28}Si^{2+}$, is not accounted since the N concentration is much lower than Si. It is assumed that all N is evaporated as $^{93}Nb^{14}N^{3+}$ within the precipitates, which is also adopted by Breen et al. [36]. TEM and high-resolution Scanning Transmission Electron Microscopy (STEM) images are acquired by JEOL Grand ARM TEM/STEM operated at 300 kV in high-angle annular dark field (HAADF) and bright field (BF) imaging modes. The corresponding elemental mapping via energy dispersive X-ray spectroscopy (EDS) was collected by the large angle dual dry solid-state 100 mm^2 detector.

Table 1
Bulk chemical compositions of the welds obtained from three different electrodes measured with OES (wt%).

Element (wt%)	C	N	O	Al	B	Cr	Cu	Mn	Mo	Nb	Ni	Si	Ti	V
Regular	0.064	0.005	0.051	0.023	<0.0002	0.15	0.191	1.45	0.18	0.049	0.1	0.25	0.006	0.003
Mn-Si rich	0.062	0.008	0.034	0.023	<0.0002	0.17	0.202	1.74	<0.00	0.052	0.1	0.47	0.006	0.004
Ti-B-Mo rich	0.054	0.008	0.036	0.02	0.003	0.16	0.186	1.59	0.17	0.05	0.1	0.3	0.023	0.004

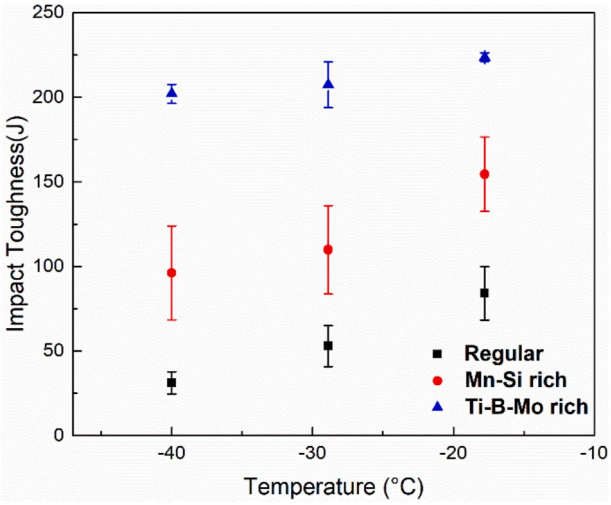

Fig. 2. Toughness comparison of the weld metal at different temperature obtained from the three types of electrodes.

3. Results and discussion

3.1. CVN impact toughness and hardness comparison

Fig. 2 compares the CVN impact toughness of the weld metal obtained from the three types of electrodes. In all the tested temperatures, Ti-B-Mo rich electrodes produce the highest toughness, followed by Mn-Si rich ones and the lowest toughness corresponds to the regular electrode. The higher amounts of Ti and B additions in welds show great improvement of the fracture toughness, which are consistent with literature findings [2]. Comparing the composition of the regular electrode and Mn-Si rich one, the Mo addition alone reduced the SAW weld toughness, as also reported in Refs. [37,38]. Average hardness was measured on the Ti-B-Mo rich and Mn-Si rich welds, where the former is around HV 225.4 with standard deviation of 6.65 and the latter is around HV 222.6 with standard deviation of 4.22. The hardness values show insignificant differences even though a superior toughness is achieved with the Ti-B-Mo rich electrode.

3.2. Optical microstructure comparison

Representative optical micrographs of the welds obtained from Mn-Si and Ti-B-Mo electrodes are compared in Fig. 3. The weld microstructure was mainly composed of acicular ferrite. Low temperature transformation microconstituents, such as upper bainite, lower bainite and Martensite-Austenite (MA) constituents are not noticed in these macrographs at lower magnification. In the Mn-Si rich weld in Fig. 3(a), appreciable portion of prior austenite grain boundary (PAGB) ferrite can be observed with an average width of 5-10 μm, as marked with the numbers. Presence of Widmanstatten ferrite (WF) along the prior austenite grain boundaries is also noticed, which has a plate-type morphology and grows into the grains in parallel arrays. Both PAGB and Widmanstatten ferrites provide favorable crack propagation paths during impact testing, promote intergranular fracture and result in underperformed toughness behavior [39,40]. In contrast, in the Ti-B-Mo rich weld, PAGB ferrite is hardly distinguishable and the PAGB shows as a line morphology in the 2D weld cross section view, as marked out in Fig. 3(b). In addition, the prior austenite grains are larger and the acicular ferrite is significantly refined with smaller grain size. The refined acicular ferrite can be a result of Ti and Mo elements, both of which facilitate acicular ferrite nucleation and formation. The naturally interlocked distribution of refined acicular ferrite and its grain boundaries serve as effective obstacles of cleavage crack propagation and

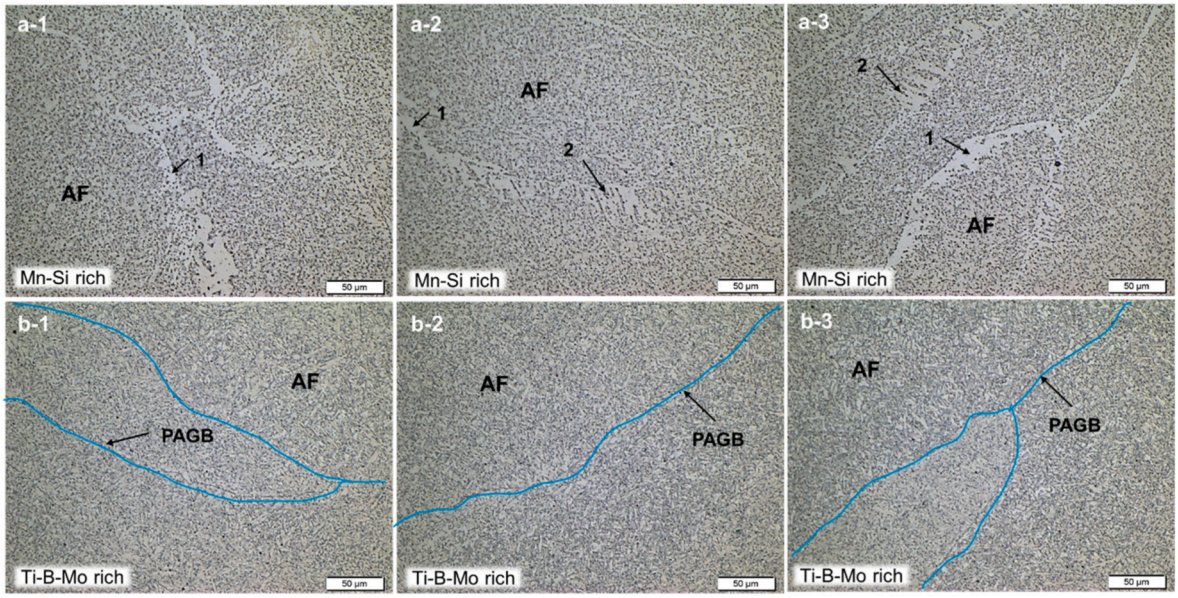

Fig. 3. Microstructure comparison (a) Mn-Si rich weld: 1: Prior austenite grain boundary ferrite 2: Widmanstatten Ferrite; (b) Ti-B-Mo rich weld, AF: acicular ferrite, PAGB: Prior austenite grain boundary.

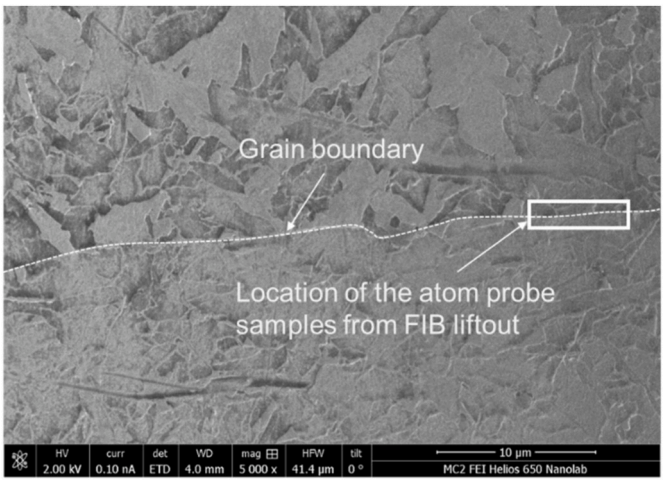

Fig. 4. Location of the atom probe samples.

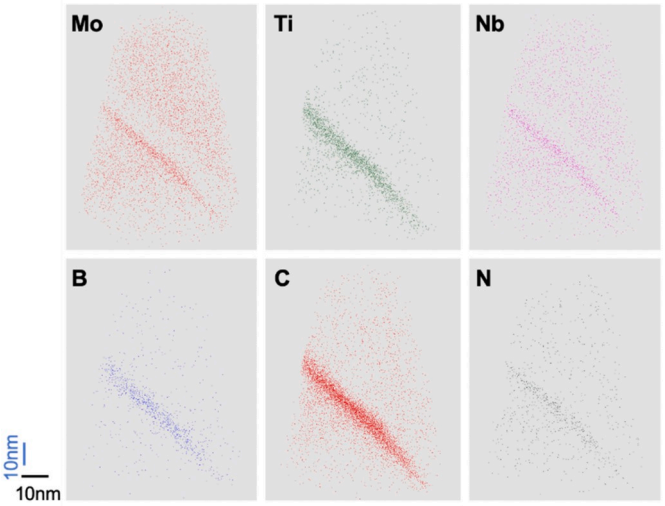

Fig. 5. 3D reconstructed atom map of the APT sample containing grain boundary.

deflect the propagation path [41,42], which accordingly enhance the weld metal toughness.

3.3. APT analysis at the prior austenite grain boundary of the weld from Ti-B-Mo rich electrode

To reveal the fundamental mechanisms of Ti, B, Mo on improving the weld metal toughness, refining the microstructure and removing PAGB ferrite, atomic resolution characterizations are performed on the welds from the Ti-B-Mo rich electrode. Fig. 4 shows the location where the APT specimens were extracted, which encloses the PAGB boundary and acicular ferrites in the vicinity. Continuous four APT samples are extracted in this region at interval distance of around 3 µm. However, since in 3D this grain boundary is not necessarily perpendicular to the weld cross section and the end diameter of the APT tip is around 40 nm, only 1 out of these 4 samples actually captures the PAGB.

Reconstructed 3D distribution of main alloying elements in the APT sample containing grain boundary is provided in Fig. 5. B, C, Ti and N are significantly enriched along the grain boundary. Presence of B inhibits nucleation of grain boundary ferrite, which agrees with the optical macrographs of the Ti-B-Mo rich welds. Segregations of Nb and Mo are to a smaller degree and a solute depleted zone adjacent to the grain boundary can be noticed. Away from the grain boundary, the amount of B is greatly reduced and all remaining elements are uniformly distributed. Precipitates and clusters of Nb are not identified in this APT sample, indicating the presence of Nb in the adjacent acicular ferrite matrix is in the form of solid solution. Li et al. [22] observed Nb segregation at the PAGB boundary and explained diffusion of Nb relies on the vacancy flux. According to Faulkner [43], the binding energy between a vacancy and B and Nb are approximately 0.48 eV and 0.42 eV. This suggests the available vacancies are preferentially occupied by other elements first, for example B, then Nb. Accordingly, in this studied weld metal, the level of Nb segregation is limited at PAGB and a higher portion of Nb stays in the ferrite matrix.

Fig. 6 provides 1D quantitative concentration profiles of different alloying elements along the direction normal to the grain boundary plane, measured with a bin size of 0.5 nm. In these analyses, a certain amount of H atoms are always noticed as hydrogen is a common gas contained in the APT analysis chamber [44]. The 1D concentration profile again shows strong enrichments of B, C, N, Ti, Mn, and Mo at the grain boundary. Their distribution has a full width of 4-5 nm at half maximum, which are slightly broader than two atomic layers as the general grain boundary thickness. This observation is consistent with several APT results in multicomponent systems [24,45] and is potentially the result of local magnification effect that artificially enlarged the enriched zone [46]. Outside of the grain boundary, the concentrations of B, C and Ti quickly diminish to almost zero, indicating they are primarily accumulated within the grain boundary and strong affiliations exist

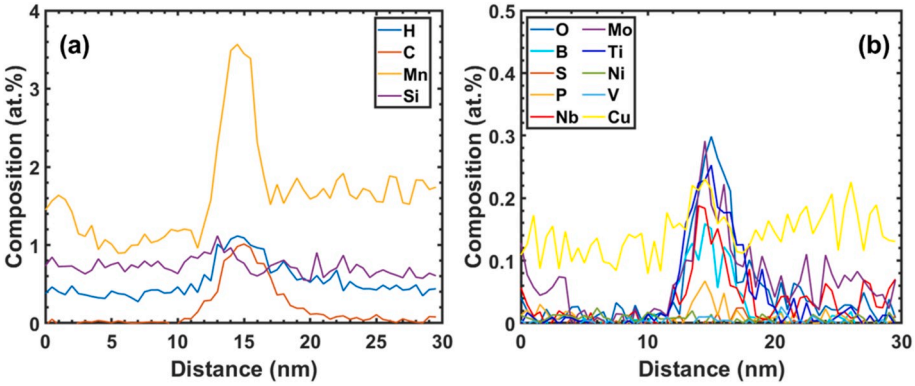

Fig. 6. 1D concentration profile (at%) of different alloying elements along the normal direction of grain boundary plane (a) Elements with peak concentration higher than 0.5 at% (b) Elements with peak concentration lower than 0.5 at%.

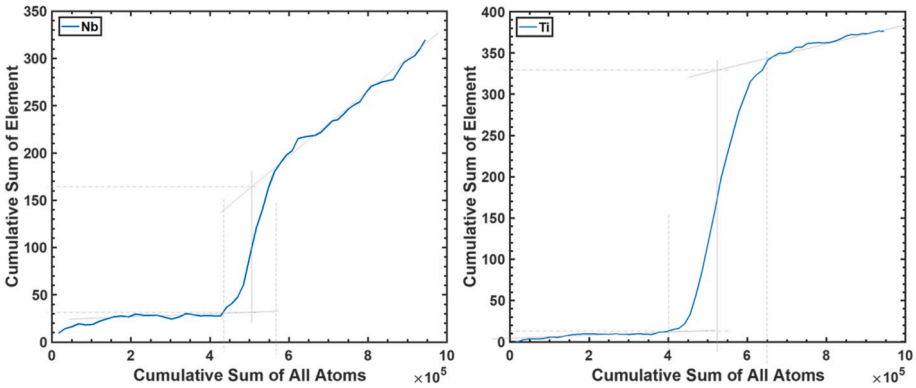

Fig. 7. Cumulative diagrams of Nb, Ti, B, Mo along the normal direction of grain boundary.

Table 2
Compositions (at%) of atom probe samples at different locations and comparison with the OES results of the bulk weld.

Element (at.%)	C	N	O	Al	B	Cr	Cu	Mn	Mo	Nb	Ni	Si	Ti	V
OES results	0.3136	0.0249	0.1570	0.0517	0.0194	0.2145	0.2037	2.0126	0.1232	0.0374	0.1184	0.7432	0.0344	0.0055
APT Tip with GB	0.1390	0.0109	0.0449	0.0009	0.0119	0.1805	0.1364	1.5899	0.0768	0.0388	0.0111	0.6293	0.0352	0.0021
Adjacent APT Tip 1	0.0245	0.0043	0.0195	0.0007	0.0014	0.1757	0.1422	1.5854	0.0880	0.0379	0.0083	0.6207	0.0056	0.0025
Adjacent APT Tip 2	0.0301	0.0048	0.0236	0.0011	0.0008	0.1780	0.1438	1.5913	0.0866	0.0354	0.0053	0.6060	0.0077	0.0024

among these elements. The extent of Nb segregation along the grain boundary is relatively small, which is similar to the findings of Felfer et al. [24]. The thermodynamically preferred reaction of C and N with Ti. In addition, reaction between Ti and N protects B at prior austenite grain boundaries. Si distribution is overall uniform throughout the entire APT tip.

The concentration of solute species at grain boundaries can be underestimated by APT to a certain extent due to the local magnification effect. Alternatively, the Gibbsian interfacial excess value is a relatively unbiased thermodynamic parameter to quantify the amount of solute-atom segregation at the grain boundary [47]. The Gibbsian interfacial excess value is defined as the number of segregated atoms divided by the area of the analyzed boundary. It can be determined from the element cumulative diagrams according to the procedure specified in Refs. [48]. Fig. 7 provides the cumulative diagrams of Nb and Ti elements for this APT sample as well as the supplementary calculation lines for determination of the interfacial excess values. Minimal slope can be observed on the curve near the grain boundary due to the solution depletion zone. Based on the cumulative diagrams, the calculated interfacial excess values for Nb, Mo, Ti and B are approximately 0.18 atom/nm^2, 0.30 atom/nm^2, 0.45 atom/nm^2, 0.24 atom/nm^2 respectively. Pronounced excess of Ti at the grain boundary can be a result of its strong affinity with B and C. The Nb interfacial excess is smaller than the one measured in an Nb-alloyed high strength low alloy steel base material while is in the same range as in its weld heat affected zone [44]. Compared with Nb interfacial excess at PAGB boundary in a strip-cast steel, which is 0.25atom/nm^2 [24], the Nb excess value in this weld metal is slightly smaller. Since the cooling rate during SAW is lower than the strip casting process, the amount of solute that was able to diffuse to this boundary should be kinetically favored and leads to a higher interfacial excess value. The opposite observation in this study is potentially the result of interactions of other alloying elements, including Ti, B and Mo that reduces the Nb segregation at the boundary.

In the mass spectrums for the other two APT samples located adjacent to the grain boundary, the B peak was hardly detected, indicating the ferrite matrix in this region is virtually free of B. Micro-chemistry of the three APT samples and macro-chemistry of the weld measured from OES are summarized in Table 2. By comparing the results, the Nb concentration in the APT dataset containing PAGB and other two APT datasets collected in the immediate proximity of PAGB, are about the same as the OES measurements. This indicates the Nb segregation is relatively insignificant at the grain boundary. Similar results can also be observed on the distribution of Mn, Mo and Si. In comparison, the contents of Ti, N, B and C are substantially reduced adjacent to grain boundary, suggesting the majority of these elements are partitioned into the boundary and their quantities in the near bulk matrix are low.

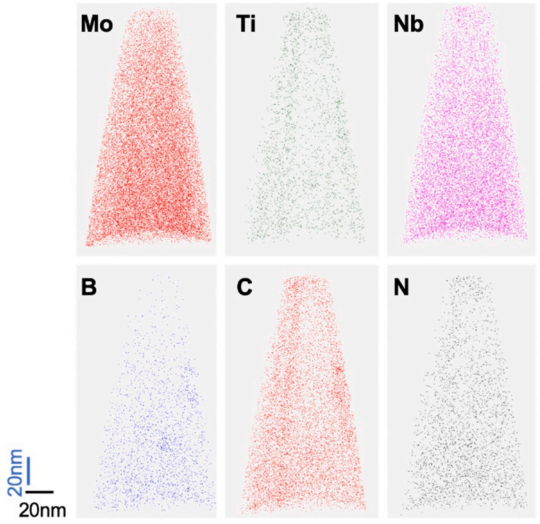

Fig. 8. 3D reconstructed atom map of the APT sample adjacent to the grain boundary.

Fig. 8 shows the 3D atom map of one of the APT samples in the vicinity of the grain boundary. It can be observed that Nb is homogeneously distributed throughout the entire detected volume. No Nb clusters or local segregation are detected, suggesting its existence in the ferrite matrix is in the form of solid solution. Other alloying elements, Mo and Ti, have similar distributions. B, C, N are also uniformly distributed regardless of their minimal contents in this APT sample.

Even though Nb has been well characterized in the steel microstructure in forms of various precipitates, its role in solid solution is still less understood. It is generally considered that the dissolved Nb in the austenite matrix suppresses the austenite-to-ferrite transformation

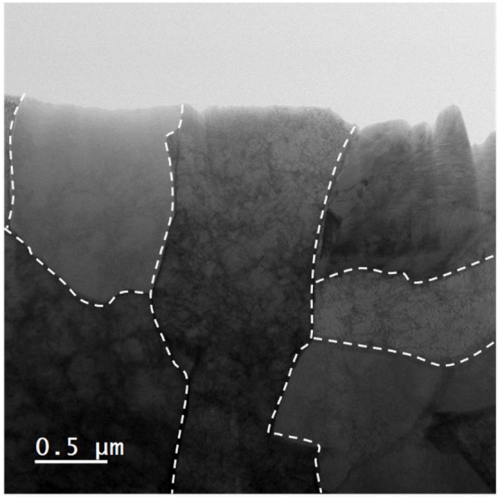

Fig. 9. Overview of the TEM sample extracted from the Ti-B-Mo rich weld.

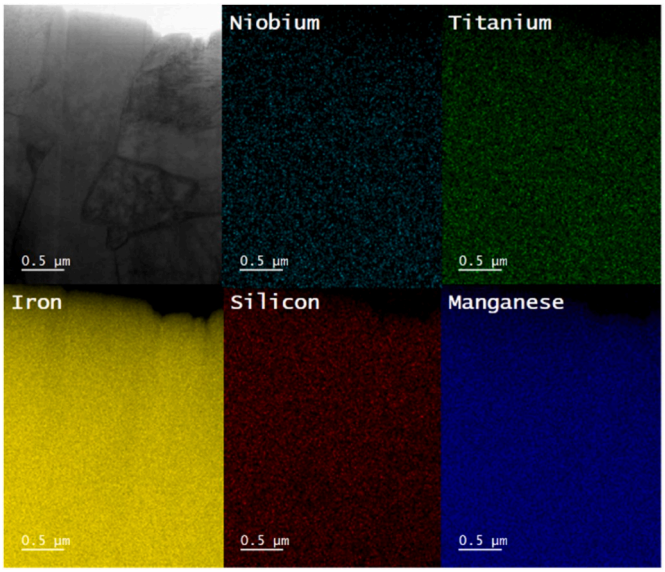

Fig. 10. EDS mapping of different alloying elements in the weld.

temperature [17,18]. Accordingly, the solid solution Nb refines the acicular ferrites microstructure, as shown in the optical micrograph of the weld from the Ti-B-Mo rich electrode in Fig. 3(b).

3.4. TEM analysis of the weld from Ti-B-Mo rich electrode

APT analysis can only provide information within a limited volume due to the sample size (generally a tip diameter of 40 nm and length of 100-200 nm), whereas the spatial resolution of SEM is incapable of identifying Nb at low concentration. Fig. 9 provides a representative TEM bright field image at a lower magnification. This TEM sample is extracted from the acicular ferrite region of the weld from the Ti-B-Mo rich electrode. The ferrite grains are separated by sharp-edged boundaries with the average size of around 1-2 μm. Dense dislocation networks and substructures can be observed within the acicular ferrite grains, which is induced by the low temperature of acicular ferrite transformation [9].

EDS elemental mapping for this region is provided in Fig. 10. Signals of Nb and Ti can be detected throughout the TEM sample and a homogenized distribution is observed at this length scale. Evidence of Nb segregation, either along the acicular ferrite grain boundaries or within the grains, is not observed. Complex (Ti, Nb)(C,N) precipitates are not detected. This agrees with the results of APT analysis that distribution of Nb and Ti in the acicular ferrite matrix are relatively uniform.

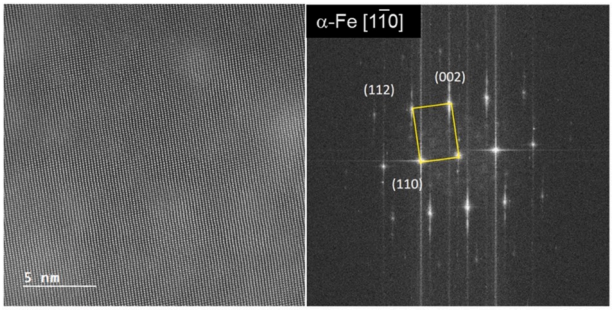

Fig. 11. (a) High resolution STEM image of the acicular ferrite matrix near PAGB (b) Corresponding indexed FFT Diffraction pattern.

To directly reveal the crystal structure and element distribution in the atomic length scale, high resolution STEM imaging within the acicular ferrite region is performed. A typical image is shown in Fig. 11, together with its FFT transformed diffraction pattern. The grain is oriented to [1$\bar{1}$0] direction and the diffraction pattern matches with the BCC crystal structure. On the other hand, the lattice spacing is slightly different from the pure ferritic iron matrix, which is potentially due to the solid solution of different alloying elements.

4. Conclusions

Combinations of Ti and B elements in the electrode produces exceptional toughness for the weld metal of Nb-alloyed steel, with predominantly refined acicular ferrite and minimal amount of prior austenite grain boundary ferrite in the weld microstructure. In this type of weld, APT analysis shows that distribution of B is highly localized in the PAGB grain boundaries, where strong enrichment of C, N and Ti are also observed. Presence of B at the grain boundary effectively prevents the formation of PAGB ferrite, as shown in the optical micrograph. Nb decorates the PAGB at a lower segregation level compared with Ti, C and B. This is potentially due to the smaller affinity of Nb to C and N compared with Ti. In the vicinity of PAGB, Nb exists in the form of solid solution in the acicular ferrite matrix without large scale segregation or precipitate formation. Similar results are also observed in TEM analysis.

Declaration of competing interest

The authors declare that they have no known competing financial interests or personal relationships that could have appeared to influence the work reported in this paper.

CRediT authorship contribution statement

Xun Liu: Conceptualization, Methodology, Validation, Investigation, Formal analysis, Writing - original draft. **Qianying Shi:** Investigation, Formal analysis, Writing - review & editing. **Mingjie Xu:** Investigation, Formal analysis. **Jiarui Kang:** Visualization, Writing - review & editing. **Sydnee Webb:** Investigation, Formal analysis.

Acknowledgement

The authors would like to appreciate the valuable technical discussions with John Procario from Lincoln Electric, Wenkao Hou and Murali Manohar from ArcelorMittal, Frank Barbaro from CBMM, as well as the metallurgical sample preparations by Mason France from OSU. The authors would like to acknowledge the Manufacturing and Materials Joining Innovation Center (Ma2JIC), from the National Science

Foundation Industry University Cooperative Research Center program (NSF/IUCRC), with the award # 1822144 for financial and/or infrastructure support. The authors would also like to acknowledge the access to the APT facility in Michigan Center for Materials Characterization at the University of Michigan and TEM facilities provided by the University of California, Irvine Materials Research Institute (IMRI).

References

[1] J.M. Gray, H. Stuart, Development of Superior Notch Toughness in High-Dilution Weldments of Microalloyed Steel, Welding Research Council, 1981.
[2] Liebeherr, M., Güngör, Ö. E., Sanchez, N., Luccioni, H., and Ilic, N., "Recommendations for submerged arc spiral welding with optimized CTOD properties," Proc. 2018 12th International Pipeline Conference, American Society of Mechanical Engineers, pp. V003T005A039-V003T005A039.
[3] B. Loberg, A. Nordgren, J. Strid, K. Easterling, The role of alloy composition on the stability of nitrides in Ti-microalloyed steels during weld thermal cycles, Metall. Trans. A 15 (1) (1984) 33–41.
[4] S. St-Laurent, G. L'Espérance, Effects of chemistry, density and size distribution of inclusions on the nucleation of acicular ferrite of C- Mn steel shielded-metal-arc-welding weldments, Mater. Sci. Eng., A 149 (2) (1992) 203–216.
[5] Fairchild, D., Macia, M., Bangaru, N., Koo, J., Ozekcin, A., and Jin, H., "Welding development for the world's strongest pipeline: X120'," Proc. 7th Int'l Conf. on Trends in Welding Research.
[6] Y. Kang, S. Jeong, J.-H. Kang, C. Lee, Factors affecting the inclusion potency for acicular ferrite nucleation in high-strength steel welds, Metall. Mater. Trans. 47 (6) (2016) 2842–2854.
[7] B. Beidokhti, A. Koukabi, A. Dolati, Effect of titanium addition on the microstructure and inclusion formation in submerged arc welded HSLA pipeline steel, J. Mater. Process. Technol. 209 (8) (2009) 4027–4035.
[8] M. Fattahi, N. Nabhani, M. Hosseini, N. Arabian, E. Rahimi, Effect of Ti-containing inclusions on the nucleation of acicular ferrite and mechanical properties of multipass weld metals, Micron 45 (2013) 107–114.
[9] Barbaro, F., and Krauklis, P., "Intragranular ferrite in inoculated low-carbon steels," Proc. Materials Forum, pp. 77-104.
[10] F.B. Pickering, Physical Metallurgy and the Design of Steels, Applied Science Publishers, London, 1978.
[11] L. Karlsson, H. Norden, H. Odelius, Overview no. 63 Non-equilibrium grain boundary segregation of boron in austenitic stainless steel—I. Large scale segregation behaviour, Acta Metall. 36 (1) (1988) 1–12.
[12] J. Seol, N. Lim, B. Lee, L. Renaud, C. Park, Atom probe tomography and nano secondary ion mass spectroscopy investigation of the segregation of boron at austenite grain boundaries in 0.5 wt.% carbon steels, Met. Mater. Int. 17 (3) (2011) 413–416.
[13] Y. Li, D. Ponge, P. Choi, D. Raabe, Segregation of boron at prior austenite grain boundaries in a quenched martensitic steel studied by atom probe tomography, Scripta Mater. 96 (2015) 13–16.
[14] H. Asahi, Effects of Mo addition and austenitizing temperature on hardenability of low alloy B-added steels, ISIJ Int. 42 (10) (2002) 1150–1155.
[15] G. Evans, Microstructure and properties of ferritic steel welds containing Ti and B, Weld. J. 75 (8) (1996) 251–260.
[16] T. Dorin, K. Wood, A. Taylor, P. Hodgson, N. Stanford, Effect of coiling treatment on microstructural development and precipitate strengthening of a strip cast steel, Acta Mater. 115 (2016) 167–177.
[17] Q. Yu, Z. Wang, X. Liu, G. Wang, Effect of microcontent Nb in solution on the strength of low carbon steels, Mater. Sci. Eng., A 379 (1) (2004) 384–390.
[18] Q.D. Liu, W.Q. Liu, S.J. Zhao, Solute behavior in the initial nucleation of V- and Nb-containing carbide, Metall. Mater. Trans. 42 (13) (2011) 3952–3960.
[19] F. Xiao, Y. Cao, G. Qiao, X. Zhang, L. Bo, Effect of Nb solute and NbC precipitates on dynamic or static recrystallization in Nb steels, J. Iron Steel Res. Int. 19 (11) (2012) 52–56.
[20] N. Takayama, G. Miyamoto, T. Furuhara, Chemistry and three-dimensional morphology of martensite-austenite constituent in the bainite structure of low-carbon low-alloy steels, Acta Mater. 145 (2018) 154–164.
[21] E. Essadiqi, J.J. Jonas, Effect of deformation on the austenite-to-ferrite transformation in a plain carbon and two microalloyed steels, Metall. Trans. A 19 (3) (1988) 417–426.
[22] X. Li, P. Wu, R. Yang, S. Zhao, S. Zhang, S. Chen, X. Cao, X. Wang, Nb segregation at prior austenite grain boundaries and defects in high strength low alloy steel during cooling, Mater. Des. 115 (2017) 165–169.
[23] B. Dutta, E.J. Palmiere, C.M. Sellars, Modelling the kinetics of strain induced precipitation in Nb microalloyed steels, Acta Mater. 49 (5) (2001) 785–794.
[24] P.J. Felfer, C.R. Killmore, J.G. Williams, K.R. Carpenter, S.P. Ringer, J.M. Cairney, A quantitative atom probe study of the Nb excess at prior austenite grain boundaries in a Nb microalloyed strip-cast steel, Acta Mater. 60 (13) (2012) 5049–5055.
[25] K.Y. Xie, L. Yao, C. Zhu, J.M. Cairney, C.R. Killmore, F.J. Barbaro, J.G. Williams, S. P. Ringer, Effect of Nb microalloying and hot rolling on microstructure and properties of ultrathin cast strip steels produced by the castrip «process, Metall. Mater. Trans. 42 (8) (2011) 2199–2206.
[26] K.Y. Xie, T. Zheng, J.M. Cairney, H. Kaul, J.G. Williams, F.J. Barbaro, C. R. Killmore, S.P. Ringer, Strengthening from Nb-rich clusters in a Nb-microalloyed steel, Scripta Mater. 66 (9) (2012) 710–713.
[27] C. Zhou, R. Priestner, The evolution of precipitates in Nb-Ti microalloyed steels during solidification and post-solidification cooling, ISIJ Int. 36 (11) (1996) 1397–1405.
[28] A. Craven, K. He, L. Garvie, T. Baker, Complex heterogeneous precipitation in titanium–niobium microalloyed Al-killed HSLA steels—I.(Ti, Nb)(C, N) particles, Acta Mater. 48 (15) (2000) 3857–3868.
[29] G. Tirumalasetty, M. Van Huis, C. Fang, Q. Xu, F. Tichelaar, D. Hanlon, J. Sietsma, H. Zandbergen, Characterization of NbC and (Nb, Ti) N nanoprecipitates in TRIP assisted multiphase steels, Acta Mater. 59 (19) (2011) 7406–7415.
[30] M. Kapoor, R. O'Malley, G.B. Thompson, Atom probe tomography study of multi-microalloyed carbide and carbo-nitride precipitates and the precipitation sequence in Nb-Ti HSLA steels, Metall. Mater. Trans. 47 (5) (2016) 1984–1995.
[31] Z. Jia, R. Misra, R. O'malley, S. Jansto, Fine-scale precipitation and mechanical properties of thin slab processed titanium–niobium bearing high strength steels, Mater. Sci. Eng., A 528 (22–23) (2011) 7077–7083.
[32] S. Moeinifar, A.H. Kokabi, H.R.M. Hosseini, Role of tandem submerged arc welding thermal cycles on properties of the heat affected zone in X80 microalloyed pipe line steel, J. Mater. Process. Technol. 211 (3) (2011) 368–375.
[33] R. Dolby, The influence of niobium on the microstructure and toughness of ferrite weld metal—a review, Met. Constr. 13 (11) (1981) 699–705.
[34] R. Dolby, Review of work on the influence of niobium on the microstructure and toughness of ferritic weld metal, Weld. World 19 (7) (1981) 126–140.
[35] R. Farrar, P. Harrison, Acicular ferrite in carbon-manganese weld metals: an overview, J. Mater. Sci. 22 (11) (1987) 3812–3820.
[36] A.J. Breen, K.Y. Xie, M.P. Moody, B. Gault, H.-W. Yen, C.C. Wong, J.M. Cairney, S. P. Ringer, Resolving the morphology of niobium carbonitride nano-precipitates in steel using atom probe tomography, Microsc. Microanal. 20 (4) (2014) 1100–1110.
[37] J. Procario, T. Melfi, submerged arc welding solutions for niobium micro-alloyed pipe steel–weld metal alloy systems, in: Proc. Instituto Brasileiro de Petroleo e Gas, 2011. Rio Pipeline Conference, IBP1486.
[38] S. Bhole, J. Nemade, L. Collins, C. Liu, Effect of nickel and molybdenum additions on weld metal toughness in a submerged arc welded HSLA line-pipe steel, J. Mater. Process. Technol. 173 (1) (2006) 92–100.
[39] R. Bodnar, S. Hansen, Effects of Widmanstätten ferrite on the mechanical properties of a 0.2 pct C-0.7 pct Mn steel, Metall. Mater. Trans. 25 (4) (1994) 763–773.
[40] S. Hashemi, D. Mohammadyani, M. Pouranvari, S. Mousavizadeh, On the relation of microstructure and impact toughness characteristics of DSAW steel of grade API X70, Fatig. Fract. Eng. Mater. Struct. 32 (1) (2009) 33–40.
[41] B. Hwang, Y.G. Kim, S. Lee, Y.M. Kim, N.J. Kim, J.Y. Yoo, Effective grain size and Charpy impact properties of high-toughness X70 pipeline steels, Metall. Mater. Trans. 36 (8) (2005) 2107–2114.
[42] L. Lan, X. Kong, C. Qiu, D. Zhao, Influence of microstructural aspects on impact toughness of multi-pass submerged arc welded HSLA steel joints, Mater. Des. 90 (2016) 488–498.
[43] R.G. Faulkner, Combined grain boundary equilibrium and non-equilibrium segregation in ferritic/martensitic steels, Acta Metall. 35 (12) (1987) 2905–2914.
[44] A.H. Hunter, J.D. Farren, J.N. DuPont, D.N. Seidman, An atom-probe tomographic study of arc welds in a multi-component high-strength low-alloy steel, Metall. Mater. Trans. 44 (4) (2013) 1741–1759.
[45] S.-I. Baik, M. Olszta, S. Bruemmer, D.N. Seidman, Grain-boundary structure and segregation behavior in a nickel-base stainless alloy, Scripta Mater. 66 (10) (2012) 809–812.
[46] Blavette, D., Letellier, L., Duval, P., and Guttmann, M., "Atomic-scale investigation of grain boundary segregation in Astroloy with a three dimensional atom-probe," Proc. Materials Science Forum, Trans Tech Publ, pp. 79-92.
[47] M. Guttmann, D. McLean, W. Johnson, J. Blakely, Interfacial Segregation, ASM, Metals Park, Ohio, 1979, p. 261.
[48] B.W. Krakauer, D.N. Seidman, Absolute atomic-scale measurements of the Gibbsian interfacial excess of solute at internal interfaces, Phys. Rev. B 48 (9) (1993) 6724.